J. Mech. Phys. Solids 170 (2023) 105119

Contents lists available at ScienceDirect

Journal of the Mechanics and Physics of Solids

journal homepage: www.elsevier.com/locate/jmps

An analytical model for sensing microvascular blood flow in flaps and organ grafts

Shupeng Li [a], Di Lu [b,c], Mitchell Pet [d], John A. Rogers [a,b,e,f,g], Yonggang Huang [a,b,e,h,*]

[a] Department of Mechanical Engineering, Northwestern University, Evanston, IL, USA
[b] Querrey Simpson Institute for Bioelectronics, Northwestern University, Evanston, IL, USA
[c] School of Microelectronics, University of Science and Technology of China, Hefei, Anhui, China.
[d] Division of Plastic and Reconstructive Surgery, Washington University School of Medicine, St Louis, MO, USA
[e] Department of Materials Science and Engineering, Northwestern University, Evanston, IL, USA
[f] Department of Biomedical Engineering, Northwestern University, Evanston, IL, USA
[g] Department of Neurological Surgery, Feinberg School of Medicine, Northwestern University, Chicago, IL, USA
[h] Departments of Civil and Environmental Engineering, Northwestern University, Evanston, IL, USA

ARTICLE INFO

Keywords:
Flow sensing
Heat conduction
Heat convection
Thrombosis diagnosis

ABSTRACT

Thrombosis after free flap transfer or solid organ allotransplantation surgeries can lead to flap or organ failure requiring re-transplantation and sometimes leading to death. Current technologies can provide early warnings of thrombosis, but the resulting measurements can be influenced by motions associated with route operations in patient care and by subtle aspects associated with the use of the devices. These systems also require wired interfaces to external data acquisition hardware, which limits patient mobility and subject the sensor to artefact from interface disruption attributable to external tension. Furthermore, many existing systems require that the probe be mounted directly on the anastomosed artery or vein which puts these delicate structures at risk for kinking, avulsion, or other disruption. Recent reports describe a wireless, implantable flow sensing probe technology that exploits thermal transport mechanisms to enable continuous monitoring of microvascular flow velocity within peripheral tissue that is remote from the critical blood supply. The capability is useful for the reliable detection of thrombosis in auto- or allo-transplanted flaps or organs. Because the probe directly measures temperature rather than flow velocity, analytical models must be used to interpret the results. Here, such a model, accounting for both heat conduction and heat convection (due to blood flow), is developed to determine the blood flow velocity in flaps and organ grafts for this flow sensing probe. The model is validated by *in vitro* experiments without and with blood flow and further applied to *in vivo* experiments to predict the flow velocity. The model serves as an important support for this type of flow sensing probe and ensures reliable and accurate flow monitoring after the transplantation operations.

1. Introduction

Free flap transfer and solid organ allotransplantation are key procedures to treat the loss or dysfunction of a vital body part

* Corresponding author.
E-mail address: y-huang@northwestern.edu (Y. Huang).

https://doi.org/10.1016/j.jmps.2022.105119
Received 1 September 2022; Received in revised form 20 October 2022; Accepted 21 October 2022
Available online 28 October 2022

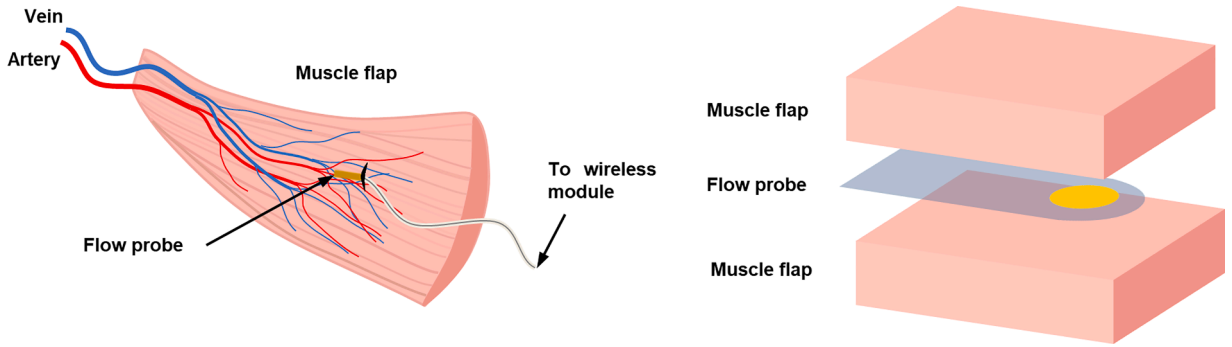

Fig. 1. Schematic muscle flap model with the flow probe inserted.

(Novakovic et al., 2009). The success of free tissue transfer depends upon harvest of the flap or organ along with its critical artery and vein, followed by surgical anastomosis to nearby vessels at the recipient site. A common mode of early post-operative failure mechanism is thrombosis (blood clotting), which occurs in 5–10% flaps (Askari et al., 2006; Chen et al., 2007). The vast majority of these failures occur within 48 h of surgical transfer (Kroll et al., 1996; Chen et al., 2007). When thrombosis is detected early, reoperation and surgical salvage is facilitated, and can be life or limb-saving. Delayed detection of thrombosis generally results in necrosis of the flap or organ graft, which is a devastating event.

For monitoring of the microsurgical free flap, traditional methods are mostly empirical and qualitative (Hirigoyen et al., 1995; Spiegel and Polat, 2007), reliant on intermittent assessments of flap color, turgor, bleeding after pinprick, capillary refill or external doppler signal. More recently, continuous quantitative monitoring methods have emerged, based on implanted doppler probes that wrap around the pedicle vessels, and near-infrared spectroscopy (NIRS) techniques that measure regional tissue oxygenation (StO_2) (Keller, 2007, 2009). These continuous methods have gained some clinical acceptance, but their utility is limited by inconsistencies associated with venous/ arterial or cutaneous mounting (Poder and Fortier, 2013). Furthermore, their requirements for wired operation restrict patient mobility and introduce other complications related to the potential for tissue damage. In addition, the NIRS devices cannot be applied to muscle or buried flaps due to the absence of an exposed skin paddle (Kozusko and Gbulie, 2018) for mounting.

For solid organ transplants buried in the thorax, peritoneum or retroperitoneum, direct monitoring is difficult, and implanted Doppler probes have poor responsiveness to any insult aside from complete vascular occlusion (Amdisen et al., 2017). In spite of drawbacks similar to those of the methods described previously, intermittent Doppler duplex ultrasound remains the main strategy to identify anastomosed arteries and veins extracorporeally and to determine the vascular flow velocities (Lorenzetti et al., 1999; Spiegel and Polat, 2007).

Implantable thermal microvascular flow probes can operate with rapid responses in almost all soft tissues, without the need to contact the source vessels (Arkin et al., 1994). Together with calibrated theoretical models, measurements of the thermal conductivity and diffusivity (Chen et al., 1981; Valvano et al., 1985; Bronzino and Peterson, 2018) performed with these technologies can yield accurate estimates of perfusion in *ex vivo* organs (Valvano et al., 1984; Anderson et al., 1992) and in *in vivo* cerebral tissues (Rosenthal et al., 2011). Existing devices of this type are wired and connected to semi-permanent skeletal features to allow stable measurements (Rosenthal et al., 2011). The results are, however, still influenced by thermal or mechanical disturbances that cause baseline drifts. These effects lead to difficulties in distinguishing normal and thrombotic phases (Jaeger et al., 2005). Also, heaters in previously reported probes and theoretical models apply only to 3-dimensional (3D) spherical shapes (Khot et al., 2005) that are not optimized for sensing performance.

Perfusion or microvascular flow velocity are the most important diagnostic parameters for arterial or venous thrombosis. Recent advances in wireless, bio-integrated electronic systems serve as a promising basis for developing devices for continuous monitoring of blood flow velocity (Klinker et al., 2015; Webb et al., 2015; Krishnan et al., 2020; Wang et al., 2021). Most such devices are, however, skin-interfaced and fail to detect processes at depths of tissues or at the locations of organs inside the body; other implanted devices operate inside arteries but cannot be easily adapted for use in monitoring microvascular flow due to size limitations. Lu et al. (Lu et al., 2022) recently reported a wireless flow sensing system that overcomes these limitations through the use of flexible device designs and biodegradable materials. The result enables continuous flow velocity and/or perfusion measurements and early, reliable detection of arterial or venous thrombosis in muscle free flaps and allotransplanted solid organs. The system includes an implantable probe for microvascular flow measurements based on thermal transport, and a wireless communication module as shown in Fig. 1. The probe is miniaturized to minimize tissue damage during insertion, with a thin circular-shaped heater (instead of 3D spherical shape) integrated onto one end of the probe. The probe measures temperature and a theoretical model establishes a quantitative connection to flow velocity. Such a model, accounting for both heat conduction and heat convection (due to blood flow), is developed in Section 2 for this flow sensing system. The model is validated by finite element analysis (FEA) and *in vitro* experiments in Section 3. The model is further validated by, and applied to, *in vivo* experiments in Section 4, which also shows a universal relation between the normalized temperature and flow velocity.

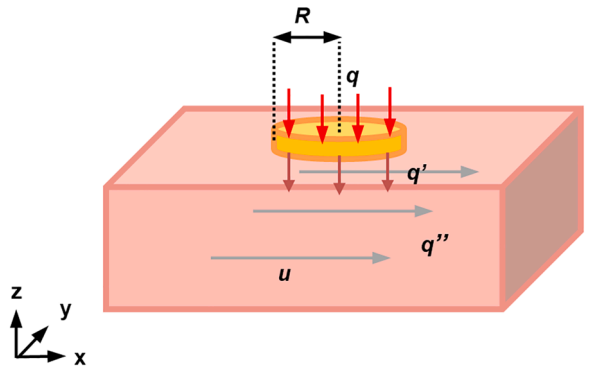

Fig. 2. Schematic diagram of the analytical model.

2. An analytical model for flow sensing

2.1. Model

Flaps or organs consist of tissues and biofluids (mainly blood), treated in the following as a composite (of tissue and blood). This composite (~ 80 mm) is much larger than the flow sensing probe (~ 2 mm), such that the model can assume infinite extent, symmetric on both sides of the probe. Due to symmetry, only one side (lower half) of the composite (tissue and blood) is considered, as illustrated in Fig. 2. The heater is modeled as heat flux q over a circle of radius R on the surface. Other details of the flow probe, including the heater, will be accounted for in Section 3. In the tissue, blood flows inside capillaries with an average speed u, and the composite has a uniform (environmental) temperature before the heater is activated.[1]

The temperature measured by the device at surface is affected by both heat conduction (heat dissipation in tissue and blood) and heat convection (heat carried away by blood flow). Therefore, the heat flux q can be split into two parts (Fig. 2):

$$q\pi R^2 = q'\pi R^2 + q'' S_{\text{capillaries}}, \tag{1}$$

where q' (to be determined) is the effective heat flux for heat conduction into the composite (of tissue and blood), $q''S_{\text{capillaries}}$ is the heat carried away by blood flow, q'' (to be determined) is the corresponding heat flux, which decreases with the flow velocity and vanishes for stationary fluid (zero flow velocity), and the net area of capillaries $S_{\text{capillaries}}$ under the heater is related to blood content s (volume fraction of blood in the tissue) by $S_{\text{capillaries}} = s\pi R^2$. Eq. (1) then becomes $q = q' + sq''$. This mechanism accounts for both heat conduction and heat convection. The analytical model below will give q'' analytically in terms of the flow velocity, therefore relate the flow velocity to the measured temperature.

The characteristic time for blood flow, and therefore heat convection, is D/u, which is ~ 1 s for the heater diameter $D = 1.5$ mm used in experiments and the flow velocity $u \sim 2$ mm/s (Fung, 2013) in capillaries. The characteristic time for heat conduction is D^2/α, which is ~ 20 s for an effective diffusivity $\alpha \sim 1 \times 10^{-7}$ m^2/s (El-Brawany et al., 2009). Since the time scale for blood flow (heat convection) is much shorter, the steady-state solution (introduced below) for convection equation can be used to estimate the heat flux reduction $q - q' = sq''$. The heating time in *in vitro* or *in vivo* experiments is at least 3 min (Lu et al., 2022), which is much longer than the time scale ~ 20 s for heat conduction such that the analysis for heat conduction is also steady state.

2.2. Heat conduction

Without blood flow, heat transfer would be only through heat conduction with the reduced heat flux $q' = q - sq''$ over the circle of radius R on the surface. Setting the origin of axisymmetric coordinates (r, z) at the center of the circle of heat flux, the steady-state heat transfer equation is (Carslaw and Jaeger, 1959)

$$\frac{\partial^2 T}{\partial r^2} + \frac{1}{r}\frac{\partial T}{\partial r} + \frac{\partial^2 T}{\partial z^2} = 0, \tag{2}$$

where T is temperature. The boundary condition on the surface is[2]

[1] Metabolic heat is neglected in the model because its heat power [~200W/m^3 (Mitchell et al., 1970)] is ~3 orders smaller than power of the heater in the experiments (~1MW/m^3).

[2] Here the adiabatic boundary condition is imposed outside the heater. This is accurate when the flow probe is inside the tissue/organ, but is approximate when the flow probe is on the surface as in *in vitro* experiments. Finite element analysis shows that its difference with the air convection boundary condition outside the heater (air convection coefficient 10 Wm^{-2}K^{-1}) is only ~ 2.8 % for the sensor temperature, therefore the adiabatic condition is a good approximation for *in vitro* experiments.

$$\begin{cases} -k\left.\frac{\partial T}{\partial z}\right|_{z=0} = q' & 0 < r < R \\ -k\left.\frac{\partial T}{\partial z}\right|_{z=0} = 0 & r > R \end{cases}, \tag{3}$$

where the effective thermal conductivity k of the composite is related to the thermal conductivities of its constituents k_{tissue} and k_{blood} via the Behrens model (Progelhof et al., 1976), $k = k_{\text{tissue}}\frac{(p+2)+2s(p-1)}{(p+2)-s(p-1)}$, and $p = k_{\text{blood}}/k_{\text{tissue}}$; and k equals k_{tissue} and k_{blood} for $s = 0$ and $s = 1$, respectively. The environmental temperature is imposed at the remote boundary. In the following let T denote the temperature difference from the environmental temperature such that T approaches zero at infinity. For the surface heat flux q', T has the solution (Carslaw and Jaeger, 1959)

$$T = \frac{q'R}{k}\int_0^\infty e^{-\lambda|z|}J_0(\lambda r)J_1(\lambda R)\frac{d\lambda}{\lambda}, \tag{4}$$

where J_0 and J_1 are Bessel functions of the first kind for integer orders of 0 and 1, respectively. The surface temperature ($z = 0$) is given by

$$T_{\text{surface}} = \frac{q'R}{k}\int_0^\infty J_0(\lambda r)J_1(\lambda R)\frac{d\lambda}{\lambda}. \tag{5}$$

Its average over the heater area is

$$\overline{T}_{\text{surface}} = \frac{\int_0^R T 2\pi r dr}{\pi R^2} = \frac{8q'R}{3\pi k}. \tag{6}$$

2.3. Heat convection

The heat flux carried away by blood flow is q''. Let x be the local direction of blood flow in each capillary (Fig. 2). The steady-state heat convection equation is (Nield and Bejan, 2006)

$$u\frac{\partial T}{\partial x} = \alpha_{\text{fluid}}\left(\frac{\partial^2 T}{\partial x^2} + \frac{\partial^2 T}{\partial y^2} + \frac{\partial^2 T}{\partial z^2}\right), \tag{7}$$

where T is the temperature change from the uniform value in remote field, α_{fluid} is the thermal diffusivity of blood, z is normal to the surface and y is normal to both z and x (flow) directions as shown in Fig. 2. The heater on tissue surface, together with blood flow, create a rapid temperature change right below the heater from the surface to inside the tissue, i.e., a thermal boundary layer (Bergman et al., 2011). Outside the heater the temperature changes slowly, i.e., no boundary layer. The temperature gradient along the layer thickness direction z dominates, i.e., $\frac{\partial^2}{\partial z^2}$ overwhelms $\frac{\partial^2}{\partial x^2}$ and $\frac{\partial^2}{\partial y^2}$, within the boundary layer, therefore the steady-state heat convection equation can be simplified to

$$u\frac{\partial T}{\partial x} = \alpha_{\text{fluid}}\frac{\partial^2 T}{\partial z^2}. \tag{8}$$

It has the solution (Nield and Bejan, 2006)

$$T = \overline{T}_{\text{surface}}\left[1 - \text{erf}\left(\frac{z}{2}\sqrt{\frac{u}{\alpha_{\text{fluid}}x}}\right)\right], \tag{9}$$

where $\overline{T}_{\text{surface}}$ is the average change of surface temperature (at $z = 0$), and erf is the error function. The thickness of boundary layer, determined by the temperature change reaching 1% of $\overline{T}_{\text{surface}}$ (Nield and Bejan, 2006), i.e.,$T = 0.01\overline{T}_{\text{surface}}$, is determined from the error function as $3.6\sqrt{\frac{\alpha_{\text{fluid}}x}{u}}$. The local heat flux into the boundary layer, in order to sustain the surface temperature change $\overline{T}_{\text{surface}}$, is $0.56\sqrt{\frac{u}{\alpha_{\text{fluid}}x}}k\overline{T}_{\text{surface}}$ (Nield and Bejan, 2006). The average heat flux over a representative length L, i.e., $\int_0^L 0.56\sqrt{\frac{u}{\alpha_{\text{fluid}}x}}k\Delta T_{\text{boundary}}dx/L$, gives

$$q'' = 1.1\sqrt{\frac{u}{\alpha_{\text{fluid}}L}}k\overline{T}_{\text{surface}} = 0.90\sqrt{\frac{u}{\alpha_{\text{fluid}}R}}k\overline{T}_{\text{surface}}. \tag{10}$$

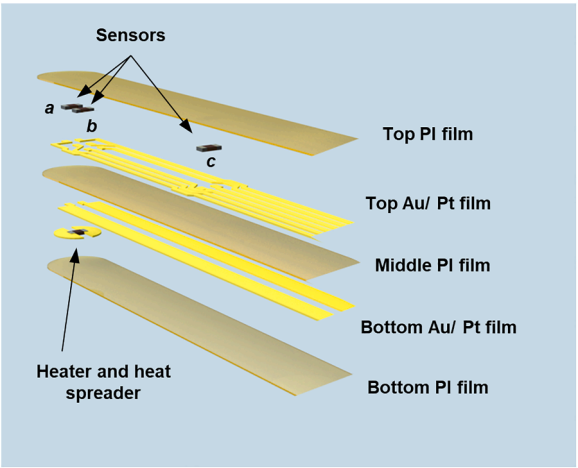

Fig. 3. Exploded view for the flow probe.

For the circular heater of radius R, the length L of capillaries ranges from 0 to $2R$, and its average is $L = \pi R/2$. As blood flow in all capillaries has the same effect to reduce the heat flux into the composite, Eq. (10) holds approximately with $L = \pi R/2$.

2.4. Analytical relation between surface temperature and flow velocity

The reduced effective heat flux $q^{'}$, sq'' and $\overline{T}_{\text{surface}}$ are solved from Eqs. (1), (6) and (10) as

$$q^{'} = \frac{q}{1 + 0.76s\sqrt{\frac{uR}{\alpha_{\text{fluid}}}}}, \tag{11}$$

$$sq'' = \frac{sq}{s + 1.3\sqrt{\frac{\alpha_{\text{fluid}}}{uR}}}, \tag{12}$$

$$\overline{T}_{\text{surface}} = \frac{8R}{3\pi k}\frac{q}{1 + 0.76s\sqrt{\frac{uR}{\alpha_{\text{fluid}}}}}. \tag{13}$$

For $s = 0$ (no blood) or $u = 0$ (no blood flow), sq'' is zero and $q^{'}$ is simply the total heat flux q. As the flow velocity u increases, sq'' also increases (more heat taken away by blood flow) and approaches the total heat flux q for very large u. For representative parameters in experiments (Lu et al., 2022), the heat carried away by blood flow is a non-negligible portion of the total heat from the heater; the ratio $\frac{sq''}{q}$ is $\sim 10\%$ for *in vitro* experiments and $\sim 40\%$ for *in vivo* experiments (Lu et al., 2022), which shows the importance of accounting for the heat carried away by blood flow.

The temperature distribution on tissue surface in Eq. (5) is then given by

$$T_{\text{surface}} = \frac{qR/k}{1 + 0.76s\sqrt{\frac{uR}{\alpha_{\text{fluid}}}}} F\left(\frac{r}{R}\right), \tag{14}$$

where $F\left(\frac{r}{R}\right) = \int_0^\infty J_0(\lambda r)J_1(\lambda R)\frac{d\lambda}{\lambda}$. For the limits of no blood ($s = 0$) or no blood flow ($u = 0$), the above equation degenerates to the classic heat conduction solution in Eq. (5) with $q^{'}$ replaced by q. For non-zero u, the above equation determines the flow velocity u from the measured T_{surface}, if the blood content s is known in the experiments.

3. Specimen calibrations and experimental validations

3.1. Detailed structures of the flow probe (Lu et al., 2022)

The flow probe consists of 7 layers from bottom (contacting with tissue) to top (free surface) as shown in Fig. 3. The first, fourth and seventh layers are polyimide (PI) films with same thickness of 75 μm. A heater, which has a box size ($0.6 \times 0.32 \times 0.4$ mm^3) is in one end of the second layer (thickness 0.4 mm). A circular gold film (diameter 1.5 mm, thickness 25 μm) is around the heater and its top surface is in the same level as heater's top surface. The rest of the second layer is filled with epoxy. Inert, biocompatible traces of noble

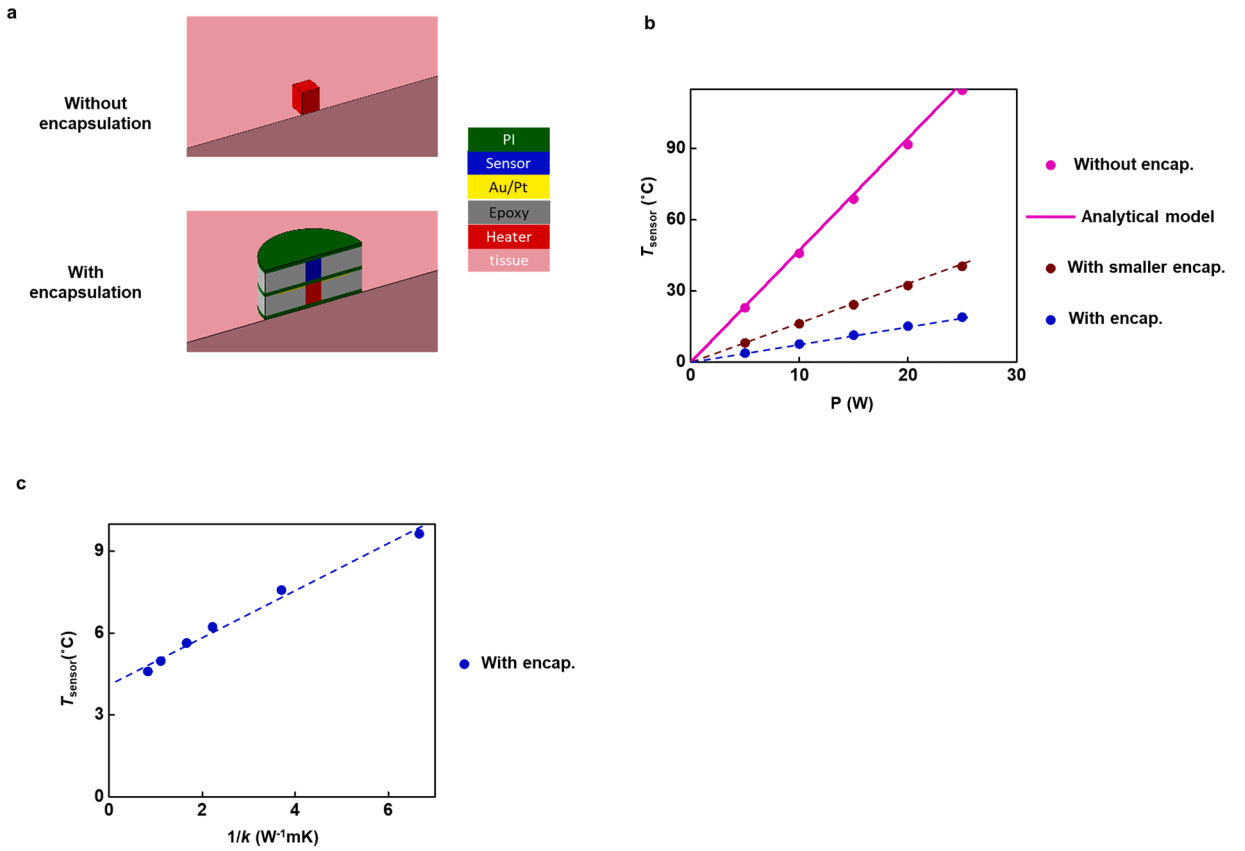

Fig. 4. (a) Sectional view of FEA models for the flow probe without and with the encapsulation layers; (b) sensor *a* temperature versus heat power with/ without encapsulation; (c) sensor *a* temperature versus the reciprocal of composite conductivity with encapsulation.

metals (Au/Pt, 50/300 nm) are in the third and fifth layers (thickness 350 nm) to form interconnects to the heater in the second layer and sensors in the sixth layer, respectively. Several surface-mount negative temperature coefficient (NTC) sensors, *a*-*c*, which have the same sizes as the heater, are at different positions along the length of the probe in the sixth layer (thickness 0.4 mm), which is also filled with epoxy. Sensor *a* is right above the heater, and sensors *b* and *c* have the distance 0.75 mm and 8 mm to sensor *a*, respectively. The cross section of the probe is 2 mm wide.

Compared to the experimental setup, the analytical model in the previous section has not accounted for some details:

1) Vertically (*z* direction), the model neglects the encapsulation layers (PI/metal/epoxy films) above the tissue, nor the box shape of the heater and sensors, therefore heat conduction through encapsulation layers is not accounted for;

2) Horizontally (*x*-*y* plane), the encapsulation layers (PI/metal/epoxy films) extend far beyond the circle (radius *R*) of heat flux used to model the heater, and these encapsulation layers also contain metal interconnects, which further dissipate heat outside the circle therefore reduce the heat flux into the tissue.

Based on the finite element analysis (FEA) and the *in vitro* experiments without blood flow ($u = 0$), the analytical model is modified in this section to account for the details of experiments discussed above.

3.2. Finite element analysis

FEA is used to account for the above detailed structures of the flow probe neglected in the analytical model in Section 2. It focuses on the steady-state heat conduction in the tissue without blood flow. A volume heat power P is imposed to the heater, and its baseline value is $P = 10$ mW. Eight-node linear heat transfer elements (DC3D8) in the commercial software ABAQUS are used, with refined mesh near the heater (total ~ 600,000 elements) to ensure convergence. The heat conductivities are $k_{PI} = 0.12$ $Wm^{-1}K^{-1}$ for PI (value supplied by the manufacturer), $k_{Au} = 310$ $Wm^{-1}K^{-1}$ for gold, $k_{Pt} = 78$ $Wm^{-1}K^{-1}$ for platinum and $k_{epoxy} = 0.2$ $Wm^{-1}K^{-1}$ for epoxy (Shimamura et al., 2020), and the baseline value of the effective conductivity $k = 0.27$ $Wm^{-1}K^{-1}$ for the composite of tissue and blood.

Fig. 4a shows the schematic diagrams of the heater on the tissue, without (top figure) and with (bottom figure) the encapsulation layers. Fig. 4b shows the linearly proportional relation between the sensor *a* temperature T_{sensor} and the heat power P for the heater without and with the encapsulation. (For the case without the encapsulation, T_{sensor} is defined by the temperature right below the heater, i.e., consistent with the analytical model in Section 2.) Without the encapsulation, the top curve in Fig. 4b obtained by FEA agrees perfectly well with the analytical model without any parameter fitting, which provide validations of both FEA and the analytical

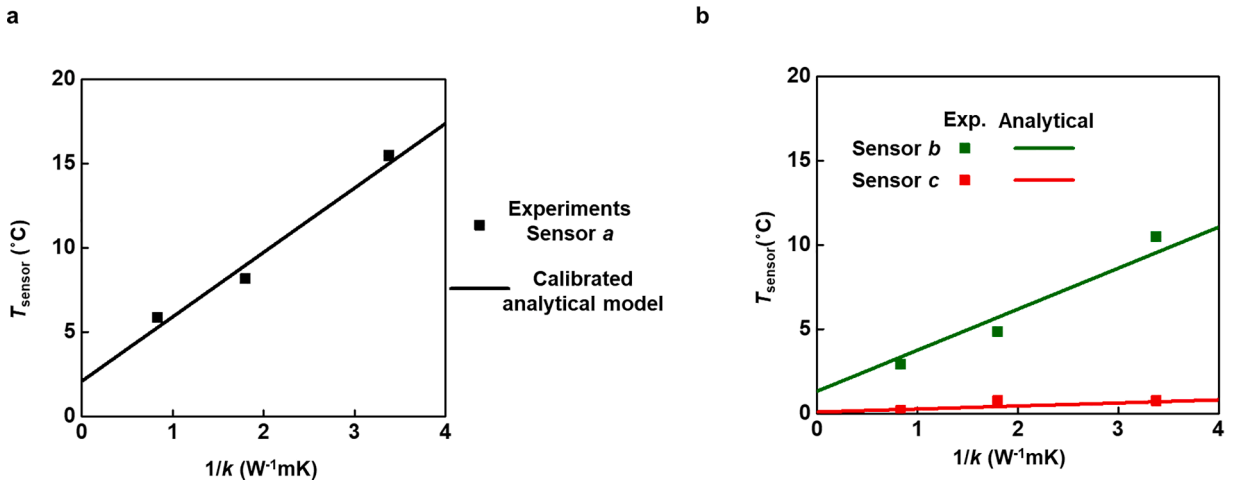

Fig. 5. (a) Calibration for the analytical model by experimental data (sensor *a*) with different composite conductivities; (b) the calibrated analytical model and the experimental data for sensors *b* and *c*.

model. Here the heat flux q in the analytical model is the heat power divided by the cross-sectional area of the heater, $q = P/(0.6 * 0.32\text{mm}^2)$, and its radius R is obtained from equivalence of the cross-sectional area as $\pi R^2 = 0.6 * 0.32\text{mm}^2$.

Fig. 4b also shows the linearly proportional relation between T_{sensor} and P for the heater with the encapsulation. The bottom line corresponds to the encapsulation in experiments, which is lower than the top line (i.e., without the encapsulation) because of the reduced heat flux into the tissue due to heat dissipation in the encapsulation. This is further illustrated by the middle line in Fig. 4b, which corresponds to the same heater but with a smaller encapsulation (radius of 1 mm); it is lower than the top line (no encapsulation), but higher than the bottom line (larger encapsulation). Therefore, the total heat flux q in Eq. (14) must be replaced by $C_{\text{calibrated}}P/(\pi R^2)$ to reflect the reduced effective heat flux into the tissue, i.e.,

$$T_{\text{surface}} = \frac{C_{\text{calibrated}}P/(\pi Rk)}{1 + 0.76s\sqrt{\frac{uR}{\alpha_{\text{fluid}}}}} F\left(\frac{r}{R}\right), \tag{15}$$

where the non-dimensional coefficient $C_{\text{calibrated}}$ is less than 1 to reflect the heat flux reduction.

Without the encapsulation, Eq. (15) suggests that the surface temperature is linearly proportional to $1/k$, therefore approaches zero in the limit $k \to \infty$. This limit is correct as $k \to \infty$, together with the remote boundary condition $T = 0$, yield zero temperature everywhere. With the encapsulation, however, Fig. 4c shows that the relation between the sensor *a* temperature T_{sensor} and reciprocal of the effective conductivity $1/k$, obtained by FEA, is linear but not linearly proportional (a straight line above the origin in Fig. 4c). This is because (1) the encapsulation layers have an effective conductivity k_{layer} (to be determined), which dissipate heat away from the tissue, and (2) the sensor is inside the encapsulation (therefore above the tissue surface) such that its temperature is not zero even for the limit of $k \to \infty$. The linear relation and the positive intercept with the vertical axis in Fig. 4c suggest that the sensor temperature is linearly proportional to $1/k + 1/k_{\text{layer}}$ such that the temperature in Eq. (15) is modified to give the sensor temperature as

$$T_{\text{sensor}} = \frac{C_{\text{calibrated}}P/(\pi R)}{1 + 0.76s\sqrt{\frac{uR}{\alpha_{\text{fluid}}}}} \left(\frac{1}{k} + \frac{1}{k_{\text{layer}}}\right) F\left(\frac{r}{R}\right) \tag{16}$$

for the flow probe on the surface of the composite (of tissue and blood), where r is the projected distance in the x-y plane between the sensor and heater, and $C_{\text{calibrated}}$ and k_{layer} are to be calibrated from experiments.

For the flow probe implanted in the composite (of tissue and blood), heat transfers to both sides of the flow probe such that Eq. (16) becomes

$$T_{\text{sensor}} = \frac{C_{\text{calibrated}}P/(\pi R)}{1 + 0.76s\sqrt{\frac{uR}{\alpha_{\text{fluid}}}}} \left(\frac{1}{2k} + \frac{1}{k_{\text{layer}}}\right) F\left(\frac{r}{R}\right), \tag{17}$$

i.e., k in Eq. (16) is replaced by $2k$.

3.3. Calibrations and validations

Calibration of $C_{\text{calibrated}}$ and k_{layer} involves the flow probe described in Section 3.1 applied to three materials at zero flow velocity $u = 0$,

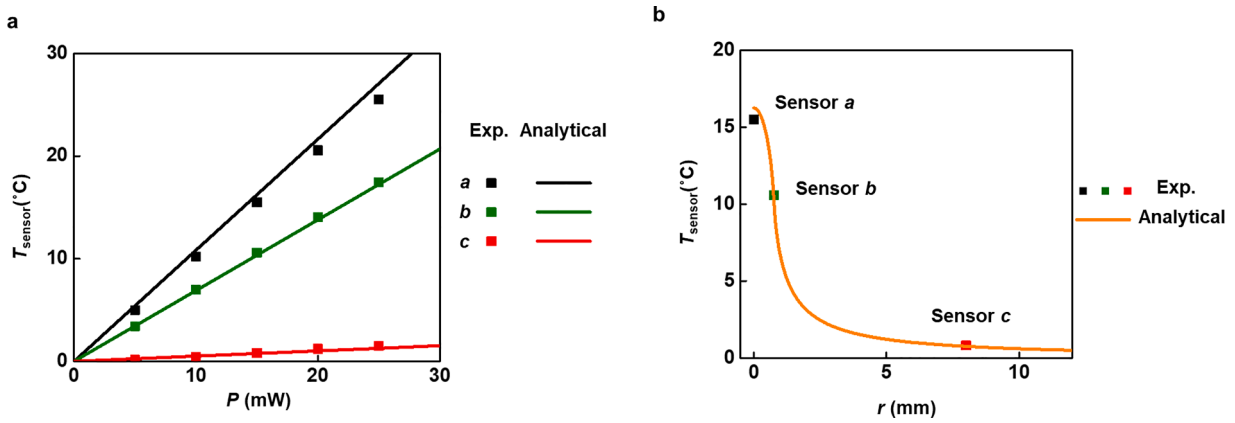

Fig. 6. The sensor temperature and the calibrated analytical model (a) versus heat power, and (b) for different sensors.

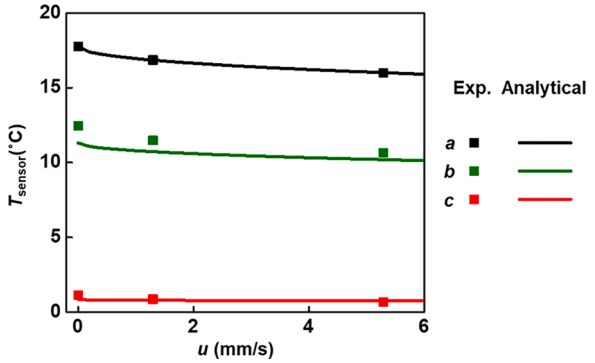

Fig. 7. The sensor temperature and the calibrated analytical model with different flow velocities.

1) flow probe on surface of a PDMS microvascular model (Lu et al., 2022) embedded with microchannels (~ 100 μm diameter, channel volume percentage $s \sim 2.5\%$) of random orientations [thermal conductivity $k = 0.27$ $Wm^{-1}K^{-1}$ (value supplied by the manufacturer)];

2) flow probe immersed in stationary water (thermal conductivity $k = 0.6$ $Wm^{-1}K^{-1}$ (Blumm and Lindemann, 2003)); and

3) flow probe immersed in stationary 70 wt% isopropanol (thermal conductivity $k = 0.28$ $Wm^{-1}K^{-1}$ (Lu et al., 2022)).

For sensor a, at which $F = 1.0$ for $r = 0$, Eq. (16) becomes $T_{sensor} = \frac{C_{calibrated}P}{\pi R}\left(\frac{1}{k}+\frac{1}{k_{layer}}\right)$ for the PDMS microvascular model (flow probe on the surface) and $T_{sensor} = \frac{C_{calibrated}P}{\pi R}\left(\frac{1}{2k}+\frac{1}{k_{layer}}\right)$ for water and 70 wt% isopropanol (flow probe immersed in fluid). For the heat power $P = 15$ mW, Fig. 5a shows the measured temperature of sensor a versus $1/k$ for the flow probe on the surface, or versus $1/(2k)$ for the flow probe immersed in fluid, such that the above two relations become the same straight line $y = \frac{C_{calibrated}P}{\pi R}\left(x+\frac{1}{k_{layer}}\right)$ in Fig. 5a. The best fit of the experimental data to this straight line gives $C_{calibrated} = 0.60$ (i.e., 40% of heat is dissipated in the encapsulation) and $k_{layer} = 1.8$ $Wm^{-1}K^{-1}$. Here it is reasonable that k_{layer} is between the conductivities of its constituents ($k_{PI} = 0.12$ $Wm^{-1}K^{-1}$, $k_{Au} = 310$ $Wm^{-1}K^{-1}$). The effective radius R is taken as the spreader radius 0.75 mm because the spreader, having high conductivity, spreads the heat effectively over its area.

Fig. 5b shows the measured temperature of sensor b [at distance $r = 0.75$ mm, yielding $F\left(\frac{r}{R}\right) = 0.64$] and sensor c [at distance $r = 8$ mm, yielding $F\left(\frac{r}{R}\right) = 0.047$], versus $1/k$ for the flow probe on the surface [or $1/(2k)$ for the flow probe immersed in fluid]. It is clear that Eqs. (16) and (17), using the $C_{calibrated} = 0.60$ and $k_{layer} = 1.8$ $Wm^{-1}K^{-1}$ calibrated from Fig. 5a, agree perfectly with experimental results without any parameter fitting, therefore validate the analytical model.

Fig. 6a shows the measured temperature of sensors a-c versus the heat power P up to 25 mW. Without any parameter fitting they agree very well with the analytical model with $C_{calibrated} = 0.60$ and $k_{layer} = 1.8$ $Wm^{-1}K^{-1}$ calibrated from Fig. 5a. Fig. 6b shows the temperature distribution from Eq. (16) for the PDMS microvascular model (Lu et al., 2022) at the heat power $P = 15$ mW, which decreases rapidly away from the heater then gradually approaches to zero. Once again it agrees well with the sensor temperature without any parameter fitting, therefore validates function $F\left(\frac{r}{R}\right)$.

The PDMS microvascular model (Lu et al., 2022) with microchannels ($s \sim 2.5\%$) also provides validation of the analytical model accounting for the effect of fluid flow. For water ($\alpha_{fluid} = 0.14$ mm^2/s (Blumm and Lindemann, 2003)) flowing in the microchannels

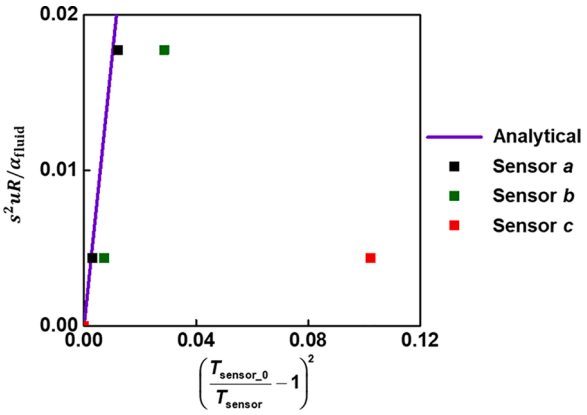

Fig. 8. The universal relation between the normalized sensor temperature and flow velocity for the analytical model and *in vitro* experimental data for different sensors.

with the controlled flow velocity up to ~ 6 mm/s, which covers the range of blood flow velocity 0.5–4 mm/s (Ivanov et al., 1981; Fung, 2013) in the capillaries, Fig. 7 shows that the temperature decreases as the flow velocity u increases. Once again, the analytical model agrees very well with the measured temperature of sensors *a-c* without any parameter fitting.

4. *In vivo* experiments and discussions

Rearrangement of Eq. (17) gives the following equation to determine the flow velocity u from the sensor temperature T_{sensor},

$$\frac{s^2uR}{\alpha_{fluid}} = 1.7\left[\frac{C_{calibrated}P/(\pi R)}{T_{sensor}}\left(\frac{1}{2k}+\frac{1}{k_{layer}}\right)F\left(\frac{r}{R}\right)-1\right]^2 = 1.7\left(\frac{T_{sensor\_0}}{T_{sensor}}-1\right)^2, \tag{18}$$

where

$$T_{sensor\_0} = \frac{C_{calibrated}P}{\pi R}\left(\frac{1}{2k}+\frac{1}{k_{layer}}\right)F\left(\frac{r}{R}\right) \tag{19}$$

is the temperature of the same sensor (i.e., at same location r) at zero flow velocity $u = 0$. Eq. (18) provides a universal relation between the normalized flow velocity $\frac{s^2uR}{\alpha_{fluid}}$ and normalized sensor temperature $\frac{T_{sensor}}{T_{sensor\_0}}$. The flow velocity u and blood content s (volume fraction of blood in the tissue) always appear together via s^2u. Therefore, the blood content s must be known in order to determine the flow velocity u by this method.

Fig. 8 shows the universal relation between the normalized flow velocity and sensor temperature in Eq. (18) by the straight line with the slope 1.7. The experimental data from Fig. 7 for the PDMS microvascular model (Lu et al., 2022) are also shown. It is clear that, for sensor a ($r = 0$), the measured data agree perfectly well with universal relation in Eq. (18) (i.e., the straight line in Fig. 8) without any parameter fitting; the agreement is reasonable for sensors b ($r = 0.75$ mm), but not well at all for sensor c ($r = 8$ mm). This is because, as indicated in Fig. 6b, the temperature decreases very fast as the distance r increases such that the relative error is large for sensors far away from the heater. Sensor a, which is closest to the heater, gives the most reliable temperature measurement.

It should be pointed out that the thermal conductivity k of the composite (of tissue and blood) may not be known for *in vivo* experiments. For a calibrated flow probe (with known $C_{calibrated}$ and k_{layer}) and a given heat power P, Eq. (19) provides an effective way to determines k from T_{sensor_0}, where T_{sensor_0} is measured by clamping artery or vein(s) to realize zero flow velocity.

The probe is implanted into a porcine muscle flap and kidney for *in vivo* experiments (Lu et al., 2022). The temperatures are monitored for three states: 1) without clamping artery and vein(s) ("released", R), 2) only clamping artery ("ischemia", I) and 3) only clamping vein(s) ("congested", C). The released state corresponds to the normal blood flow, while the ischemia and congested states correspond to arterial and venous thrombosis and immediately threaten the flap or organ viability. The purpose of the flow probe is to distinguish between the "released" state and "ischemia" or "congested" states.

The stable temperature values are collected after 15 min maintaining at each state in *in vivo* experiments (Lu et al., 2022), which give the normalized sensor temperature $T_{sensor}/T_{sensor\_0} = 0.93$, 0.98 and 0.99 for "released", "ischemia" and "congested" states in the flap, and 0.66, 0.99 and 0.99 in the kidney, respectively. Fig. 9 shows these values by the vertical dashed lines as well as the universal relation in Eq. (18) but in log scales. It is clear that the lines for the "released" state are much separated from the lines for "ischemia" and "congested" states.

With $R = 0.75$ mm and $\alpha_{fluid} = 0.14$ mm^2/s, the experimental values of T_{sensor}/T_{sensor_0}, together with Eq. (18) [or equivalently the straight lines in Fig. 8 (normal scale) or Fig. 9 (log scale)], predict the combinations of s^2u as 1.6 μm/s for the flap and 93 μm/s for the kidney at the "released" state. These values do fall into the ranges from the literature, namely 0.45–10 μm/s for the flap and 31–440 μm/s for the kidney, respectively. These large ranges result from the variations in capillary flow velocity $u = 0.5$–4 mm/s (Ivanov et al.,

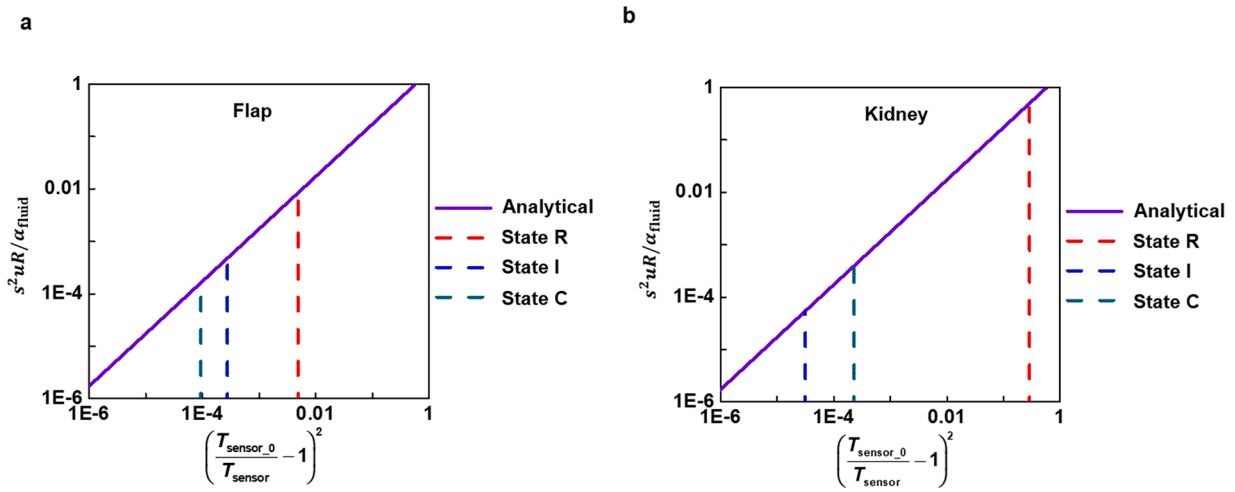

Fig. 9. The universal relation between the normalized sensor temperature and flow velocity for the analytical model (with logarithmic scale) and *in vivo* experimental data for three states [Released (R), Ischemia (I), Congested (C)] in a porcine (a) flap and (b) kidney.

1981; Fung, 2013) and blood content $s = 4\% \pm 1\%$ for flaps and $29\% \pm 4\%$ for kidneys (Linderkamp et al., 1980). For the "ischemia" state, experimental values predict the combinations of s^2u as 0.083 μm/s for the flap and 0.010 μm/s for the kidney, which are ~ 20 and ~ 9300 times smaller than the corresponding values for the "released" state, respectively. Similarly, for the "congested" state, experimental values predict s^2u as 0.010 μm/s for the flap and 0.074 μm/s for the kidney, which are also several orders of magnitude smaller than the corresponding values for the "released" state, respectively. Therefore, the value of s^2u (or equivalently the normalized sensor temperature T_{sensor}/T_{sensor_0}) falling out of the reasonable range may indicate thrombosis.

In summary, an analytical model is established to determine the blood flow velocity in flaps and organ grafts from temperatures measured using implanted flow probes. The analytical model, accounting for the effects of both heat conduction (in the tissue and blood) and convection (due to blood flow), has been validated by *in vitro* experiments without and with blood flow. Together with experiments, it can predict a combination s^2u of the flow velocity u and blood content s, and may provide a good indicator for thrombosis, which enables reliable and accurate flow sensing in free flap transfer and solid organ allotransplantation.

CRediT authorship contribution statement

Shupeng Li: Conceptualization, Methodology, Validation, Formal analysis, Investigation, Writing – original draft, Writing – review & editing, Visualization. **Di Lu:** Conceptualization, Validation, Investigation, Writing – review & editing. **Mitchell Pet:** Resources, Writing – review & editing, Supervision. **John A. Rogers:** Conceptualization, Resources, Writing – review & editing, Supervision. **Yonggang Huang:** Conceptualization, Methodology, Validation, Formal analysis, Investigation, Resources, Writing – original draft, Writing – review & editing, Visualization, Supervision, Project administration.

Declaration of Competing Interest

The authors declare that they have no known competing financial interests or personal relationships that could have appeared to influence the work reported in this paper.

Data Availability

Data will be made available on request.

Acknowledgements

S. Li gratefully acknowledges support from the Ryan Fellowship and the International Institute for Nanotechnology at Northwestern University.

References

Amdisen, C., Jespersen, B., Møldrup, U., Keller, A.K., 2017. The unsuitability of implantable Doppler probes for the early detection of renal vascular complications - a porcine model for prevention of renal transplant loss. PLoS ONE 12 (5), e0178301.
Anderson, G.T., Valvano, J.W., Santos, R.R., 1992. Self-heated thermistor measurements of perfusion. IEEE Trans. Biomed. Eng. 39 (9), 877–885.

Arkin, H., Xu, L.X., Holmes, K.R., 1994. Recent developments in modeling heat transfer in blood perfused tissues. IEEE Trans. Biomed. Eng. 41 (2), 97–107.
Askari, M., Fisher, C., Weniger, F.G., Bidic, S., Lee, W.P., 2006. Anticoagulation therapy in microsurgery: a review. J. Hand. Surg. Am. 31 (5), 836–846.
Bergman, T.L., Incropera, F.P., DeWitt, D.P., Lavine, A.S., 2011. Fundamentals of Heat and Mass Transfer. John Wiley & Sons, Hoboken, NJ, USA.
Blumm, J., Lindemann, A., 2003. Characterization of the thermophysical properties of molten polymers and liquids using the flash technique. High Temp. High Press 35 (36), 627.
Bronzino, J.D., Peterson, D.R., 2018. Molecular, cellular, and Tissue Engineering. CRC Press.
Carslaw, H.S., Jaeger, J.C., 1959. Conduction of Heat in Solids. Clarendon Press, Oxford, UK.
Chen, K.T., Mardini, S., Chuang, D.C., Lin, C.H., Cheng, M.H., Lin, Y.T., Huang, W.C., Tsao, C.K., Wei, F.C., 2007. Timing of presentation of the first signs of vascular compromise dictates the salvage outcome of free flap transfers. Plast. Reconstr. Surg. 120 (1), 187–195.
Chen, M.M., Holmes, K.R., Rupinskas, V., 1981. Pulse-decay method for measuring the thermal conductivity of living tissues. J. Biomech. Eng. 103 (4), 253–260.
El-Brawany, M.A., Nassiri, D.K., Terhaar, G., Shaw, A., Rivens, I., Lozhken, K., 2009. Measurement of thermal and ultrasonic properties of some biological tissues. J. Med. Eng. Technol. 33 (3), 249–256.
Fung, Y.C., 2013. Biomechanics: Circulation. Springer Science & Business Media, New York, USA.
Hirigoyen, M.B., Urken, M.L., Weinberg, H., 1995. Free flap monitoring: a review of current practice. Microsurgery 16 (11), 723–726.
Ivanov, K.P., Kalinina, M.K., Levkovich, Y.I., 1981. Blood flow velocity in capillaries of brain and muscles and its physiological significance. Microvasc. Res. 22 (2), 143–155.
Jaeger, M., Soehle, M., Schuhmann, M.U., Winkler, D., Meixensberger, J., 2005. Correlation of continuously monitored regional cerebral blood flow and brain tissue oxygen. Acta Neurochir 147 (1), 51–56.
Keller, A., 2007. Noninvasive tissue oximetry for flap monitoring: an initial study. J. Reconstr. Microsurg. 23 (4), 189–197.
Keller, A., 2009. A new diagnostic algorithm for early prediction of vascular compromise in 208 microsurgical flaps using tissue oxygen saturation measurements. Ann. Plast. Surg. 62 (5), 538–543.
Khot, M.B., Maitz, P.K., Phillips, B.R., Bowman, H.F., Pribaz, J.J., Orgill, D.P., 2005. Thermal diffusion probe analysis of perfusion changes in vascular occlusions of rabbit pedicle flaps. Plast. Reconstr. Surg. 115 (4), 1103–1109.
Klinker, L., Lee, S., Work, J., Wright, J., Ma, Y., Ptaszek, L., Webb, R.C., Liu, C., Sheth, N., Mansour, M., Rogers, J.A., Huang, Y., Chen, H., Ghaffari, R., 2015. Balloon catheters with integrated stretchable electronics for electrical stimulation, ablation and blood flow monitoring. Extreme Mech. Lett. 3, 45–54.
Kozusko, S., Gbulie, U., 2018. Detecting microsurgical complications with ViOptix tissue oximetry in a pediatric myocutaneous free flap: case presentation and literature review. J. Reconstr. Microsurg. Open 3 (1), e8–e12.
Krishnan, S.R., Arafa, H.M., Kwon, K., Deng, Y., Su, C.J., Reeder, J.T., Freudman, J., Stankiewicz, I., Chen, H.M., Loza, R., Mims, M., Mims, M., Lee, K., Abecassis, Z., Banks, A., Ostojich, D., Patel, M., Wang, H., Borekçi, K., Rosenow, J., Tate, M., Huang, Y., Alden, T., Potts, M.B., Ayer, A.B., Rogers, J.A., 2020. Continuous, noninvasive wireless monitoring of flow of cerebrospinal fluid through shunts in patients with hydrocephalus. NPJ Digit. Med. 3, 29.
Kroll, S.S., Schusterman, M.A., Reece, G.P., Miller, M.J., Evans, G.R.D., Robb, G.L., Baldwin, B.J., 1996. Timing of pedicle thrombosis and flap loss after free-tissue transfer. Plast. Reconstr. Surg. 98 (7), 1230–1233.
Linderkamp, O., Berg, D., Betke, K., Koferl, F., Kriegel, H., Riegel, K.P., 1980. Blood volume and hematocrit in various organs in newborn piglets. Pediatr. Res. 14 (12), 1324–1327.
Lorenzetti, F., Salmi, A., Ahovuo, J., Tukiainen, E., Asko-Seljavaara, S., 1999. Postoperative changes in blood flow in free muscle flaps: a prospective study. Microsurgery 19 (4), 196–199.
Lu, D., Li, Shupeng, Yang, Q., Arafa, H.M., Xu, Y., Yan, Y., Ostojich, D., Bai, W., Guo, H., Wu, C., Li, Shuo, Jacobson, L., Westman, A.M., Macewan, M.R., Huang, Y., Pet, M., Rogers, J.A., 2022. Implantable, wireless, self-fixing thermal sensors for continuous measurements of microvascular blood flow in flaps and organ grafts. Biosens. Bioelectron. 206, 114145.
Mitchell, J.W., Galvez, T.L., Hengle, J., Myers, G.E., Siebecker, K.L., 1970. Thermal response of human legs during cooling. J. Appl. Physiol. 29 (6), 859–865.
Nield, D.A., Bejan, A., 2006. Convection in Porous Media. Springer, New York, USA.
Novakovic, D., Patel, R.S., Goldstein, D.P., Gullane, P.J., 2009. Salvage of failed free flaps used in head and neck reconstruction. Head Neck Oncol. 1, 33.
Poder, T.G., Fortier, P.H., 2013. Implantable Doppler in monitoring free flaps: a cost-effectiveness analysis based on a systematic review of the literature. Eur. Ann. Otorhinolaryngol. Head Neck Dis. 130 (2), 79–85.
Progelhof, R.C., Throne, J.L., Ruetsch, R.R., 1976. Methods for predicting the thermal conductivity of composite systems: a review. Polym. Eng. Sci. 16 (9), 615–625.
Rosenthal, G., Sanchez-Mejia, R.O., Phan, N., Hemphill, J.C., Martin, C., Manley, G.T., 2011. Incorporating a parenchymal thermal diffusion cerebral blood flow probe in bedside assessment of cerebral autoregulation and vasoreactivity in patients with severe traumatic brain injury. J. Neurosurg. 114 (1), 62–70.
Shimamura, A., Hotta, Y., Hyuga, H., Hotta, M., Hirao, K., 2020. Improving the thermal conductivity of epoxy composites using a combustion-synthesized aggregated β-Si3N4 filler with randomly oriented grains. Sci. Rep. 10 (1), 1–9.
Spiegel, J.H., Polat, J.K., 2007. Microvascular flap reconstruction by otolaryngologists: prevalence, postoperative care, and monitoring techniques. Laryngoscope 117 (3), 485–490.
Valvano, J.W., Allen, J.T., Walsh, J.T., Hnatowich, D.J., Tomera, J.F., Brunengraber, H., Bowman, H.F., 1984. An isolated rat liver model for the evaluation of thermal techniques to quantify perfusion. J. Biomech. Eng. 106 (3), 187–191.
Valvano, J.W., Cochran, J.R., Diller, K.R., 1985. Thermal conductivity and diffusivity of biomaterials measured with self-heated thermistors. Int. J. Thermophys. 6 (3), 301–311.
Wang, F., Jin, P., Feng, Y., Fu, J., Wang, P., Liu, X., Zhang, Y., Ma, Y., Yang, Y., Yang, A., Feng, X., 2021. Flexible Doppler ultrasound device for the monitoring of blood flow velocity. Sci. Adv. 7 (44), eabi9283.
Webb, R.C., Ma, Y., Krishnan, S., Li, Y., Yoon, S., Guo, X., Feng, X., Shi, Y., Seidel, M., Cho, N.H., Kurniawan, J., Ahad, J., Sheth, N., Kim, J., Taylor, J.G., Darlington, T., Chang, K., Huang, W., Ayers, J., Gruebele, A., Pielak, R.M., Slepian, M.J., Huang, Y., Gorbach, A.M., Rogers, J.A., 2015. Epidermal Devices for Noninvasive, Precise, and Continuous Mapping of Macrovascular and Microvascular Blood Flow. Sci. Adv. 1 (9), e1500701.